# Implementation and partial validations of a non-equilibrium wall-model in an unstructured LES solver

**By G. I. Park AND P. Moin**

## 1. Motivation and objectives

Large eddy simulation (LES) solves for the large scales of turbulence directly while the smaller sub-grid scales are modeled. In order for LES to be accurate, the dynamically important motions in the flow have to be sufficiently resolved. This requirement is easily fulfilled in free shear flows where the large scales are most energetic and dynamically important. The same is not true in wall-bounded flows since the length scale of the energy-containing eddies, especially in high Reynolds number, gets progressively smaller toward the wall. Although accurate, the cost of wall-resolved LES of high Reynolds number flows approaches that of direct numerical simulation (DNS), preventing its use in wall-bounded flows of engineering applications. In order to circumvent this limitation, wall-modeled LES (WMLES) aims at predicting turbulence away from the wall using a coarse grid that does not resolve the inner layer, while modeling momentum and heat transfer across it. In WMLES, the grid spacing scales not on the viscous wall unit, but on the local boundary layer thickness. This reduces the required number of grid points from $N_{wr} \sim Re_c^{13/7}$ in wall-resolved LES to $N_{wm} \sim Re_c$ in WMLES (Choi & Moin 2012). Another factor of ten or more savings can be achieved by the use of a larger computational time step.

In WMLES, the momentum and heat fluxes at the wall ($\tau_w$ and $q_w$) are directly modeled and enter the LES domain as Neumann boundary conditions. Depending on the level of approximation in modeling these quantities, the form of the wall model can vary from simple algebraic equations to full, space-time-dependent partial differential equations (PDE). An early approach in the 1970s was to establish simple algebraic relations between the wall shear stress ($\tau_w$) and velocity data at the first off-wall LES grid point ($u_1$). These models directly apply the logarithmic law of the wall to relate $\tau_w$ to $u_1$. The assumption of a universal law of the wall is valid only in equilibrium flows, and therefore extensions to complex separated flows are not justified.

An improvement to the early wall-models was to model $\tau_w$ and $q_w$ with differential equations. The wall-model is then no longer a simple algebraic relation, and the wall fluxes are obtained by solving simplified or full RANS equations defined on an embedded, auxiliary mesh that resolves only a portion of the inner layer. The so-called equilibrium wall-model is obtained by ignoring all the terms in full RANS equations except the wall-normal diffusion. The wall-model equations then reduce to a system of uncoupled ordinary differential equations (ODE) which associate each wall face with its corresponding LES solution at the top boundary of the wall-model layer. When one retains more terms, non-equilibrium effects such as unsteadiness, nonlinear advection, and pressure gradient can be accounted for by the wall-model, at the expense of solving time-dependent PDE in three dimensions. This type of wall-model is broadly termed

a non-equilibrium wall-model. See reviews by Piomelli & Balaras (2002) and Piomelli (2008) for more comprehensive information on the wall-models described above.

In this article, we report the recent development and implementation of a non-equilibrium wall-model in an unstructured mesh environment. To authors' knowledge, none of the existing non-equilibrium wall-models has been implemented and tested in an unstructured mesh environment. This lack of implementation is not desirable for a long-term goal of applying WMLES to complex flows over or inside complex geometries. The present study therefore begins with building the framework of non-equilibrium wall-model in an unstructured flow solver. The method is similar to that of the wall-models for structured mesh described by Balaras *et al.* (1996), Cabot & Moin (2000), Wang & Moin (2002), and Kawai & Larsson (2013), but is supplemented by a new dynamic eddy viscosity/conductivity model that corrects the effect of the resolved Reynolds stress on the skin friction. Unlike earlier models, this eddy viscosity/conductivity model does not have a stress-matching procedure or a tunable free parameter, and it shows consistent performance over a wide range of Reynolds numbers.

The paper is organized as follows: Section 2 provides a description of WMLES formulation and its implementation. The proposed model is validated in Section 3, followed by the future plan in Section 4.

## 2. Implementation of a non-equilibrium wall-model in an unstructured solver

### 2.1. *Solver generic info*

The non-equilibrium wall-model is added to *Charles*, a cell-centered unstructured finite volume compressible LES solver provided by Cascade Technologies, Inc. The code is written entirely in C++, and uses domain decomposition and the Message Passing Interface (MPI) for parallelism. The base LES code is modified to enable concurrent simulation of LES and RANS, as well as communication between the two solvers. In the LES, an explicit third-order Runge-Kutta (RK3) is used for the time advancement. The spatial discretization is central and formally second-order accurate on arbitrary unstructured meshes, but reduces to a fourth-order central scheme on a Cartesian equidistant grid. For stability purposes, face reconstruction of advective fluxes is based on a convex combination of central and HLLC-upwind schemes:

$$F = (1-\alpha)F_{central} + \alpha F_{HLLC}, \tag{2.1}$$

where $0 \leq \alpha \leq 1$ is a dissipation controlling parameter proportional to the non-skew-symmetry of rows in the global advection matrix. In general, $\alpha$ is close to 1 near the hanging nodes, computational boundaries, and cells with high skewness. $\alpha$ is practically 0 on internal faces of rectangular grids. Also, $\alpha$ is set to 1 near the shock in conjunction with the use of ENO-HLLC flux reconstruction. For more detailed descriptions, see Khalighi *et al.* (2010) and Ham & Iaccarino (2004). The dynamic SGS model of Moin *et al.* (1991) with the modification of Lilly (1992) is used to calculate sub-grid scale viscosity.

The wall-model solver employs different numerical methods for solving the RANS equations: space integration using a second-order HLLC approximate Riemann solver and a backward Euler for time integration (see Pečnik *et al.* 2010). An implicit time-marching is needed to avoid a severe acoustic CFL time-step restriction caused by the wall-model mesh refined in the wall-normal direction. The maximum time step for coupled LES-RANS simulation is therefore imposed by the LES. A dynamic mixing length model described in Section 2.2 is used for the turbulence closure in the wall-model equations.

### 2.2. *Non-equilibrium wall-model*

The present non-equilibrium wall-model is based on the compressible Reynolds-averaged Navier-Stokes equations. We retain all the terms in the equations. The equations are solved on a separate wall-model mesh comprising a small sub-domain of the LES mesh ($y/\delta < 0.1$). Models for eddy viscosity ($\mu_{t,wm}$) and eddy conductivity ($\lambda_{t,wm}$) are given by

$$\mu_{t,wm} = \mu_t^* + \frac{\bar{\rho}\bar{R}_{ij}\bar{S}_{ij}^d}{2\bar{S}_{ij}^d\bar{S}_{ij}^d}, \quad \lambda_{t,wm} = \lambda_t^* + \frac{\bar{\rho}c_p\bar{G}_j\bar{Q}_j}{\bar{G}_j\bar{G}_j}, \tag{2.2}$$

where $\bar{S}_{ij}^d = \bar{S}_{ij} - 1/3\delta_{ij}\bar{S}_{kk}$ is the deviatoric part of the mean rate-of-strain tensor, $\bar{\rho}\bar{R}_{ij} = \bar{\rho}\overline{u_i'u_j'}$ is the resolved Reynolds stress, $\bar{G}_j = \partial\bar{T}/\partial x_j$ is the mean temperature gradient, $\bar{Q}_j = \overline{u_j'T'}$ is the resolved turbulent heat flux, and $c_p$ is the mass specific heat at constant pressure. The terms with superscript * are the quantities modeled with simple mixing-length models given by

$$\mu_t^* = \rho(\kappa\eta)^2|S|D(\eta), \quad \lambda_t^* = \mu_{t,wm}c_p/Pr_t, \tag{2.3}$$

where $\kappa = 0.41$ is the von Kármán constant, $Pr_t = 0.9$ is the turbulent Prandtl number, $\eta$ is the wall-normal distance, $|S| = (2\bar{S}_{ij}\bar{S}_{ij})^{0.5}$ is the magnitude of mean rate-of-strain tensor, and $D(\eta) = [1 - \exp(-\eta^+/A^+)]^2$ is the van Driest wall-damping function with $A^+ = 26$. All quantities are defined with respect to the wall-model solution, and mean (over-barred) quantities needed by the model are computed on the fly by defining an appropriate temporal averaging operator.

The motivation for developing the above model comes from the fact that the use of steady RANS type model (Eq. (2.3)) in unsteady nonlinear equations causes persistent overprediction of skin friction. Cabot & Moin (2000) claimed that the eddy viscosity in the wall-model equation should account only for the unresolved part of the Reynolds stress, since the resolved stress carried by the nonlinear advection terms in the RANS equations is not negligible. Wang & Moin (2002) showed that the inclusion of the non-linear terms in the wall-model equation increases the wall stress. In order to compensate for this effect, they reduced the value of eddy viscosity in the wall-model equation by dynamically matching the total turbulent stress (resolved + modeled) in the LES and the wall-model at the matching location. Kawai & Larsson (2013) recently showed that the aforementioned dynamic approach at high Reynolds number yielded too low eddy viscosity throughout the wall-model layer, resulting in significantly underpredicted wall shear stress. In the same paper, they proposed an eddy viscosity model in which the von Kármán constant has an assumed linear variation in the wall-normal direction, with its slope adjusted by a tuning parameter.

The proposed models in Eq. (2.2) are derived by directly requiring the turbulence model to account only for the unresolved part of the Reynolds stress. A more intuitive derivation in incompressible limit is to directly obtain the eddy viscosity of the resolved motion ($\mu_t^r$) from the resolved turbulent energy production ($P^r \equiv -\bar{\rho}\bar{R}_{ij}\bar{S}_{ij} = 2\mu_t^r\bar{S}_{ij}\bar{S}_{ij}$), and then to subtract it from $\mu_t^*$. It can be shown that the $-\mu_t^r$ obtained from this relation is identical to the additive term in the right-hand side of Eq. (2.2) for $\mu_{t,wm}$. For complete derivations omitted here, we refer to Park & Moin (2014). The model is dynamic in the sense that the model coefficients are determined automatically from the wall-model solution only, and without using tuning parameters. As reported in Section 3, the model shows consistent performance over a wide range of Reynolds numbers.

### 2.3. *Boundary conditions*

The LES and the wall-model exchange boundary conditions (BC) at each time step. The wall BC required by the LES is provided by the wall-model in terms of flux BC. In the cell-centered finite volume formulation, the information needed by a wall-adjacent cell is $\sigma_{ij}$ and $q_j$ at the wall face, where $\sigma_{ij}$ is the viscous stress tensor and $q_j$ is the heat flux vector. These quantities are reconstructed from the wall-model solution near the wall. The obvious kinematic no-penetration condition is still maintained. Top BC of the wall-model equations are imposed by the LES solution at the corresponding matching location in terms of primitive variables ($\rho$, $u_i$, $p$). A no-slip condition is applied at the wall, since the wall-model mesh is designed to resolve the viscous sublayer in the wall-normal direction.

Implementation of the BC communication routine in an unstructured parallel solver requires some effort, since logically ordered connectivity is not available and the faces involved in information exchange likely reside on different processors with different face indices. The situation gets more complicated when some of the faces involved in the BC communication are not shared between the two solvers. For example, when the LES mesh is composed of tetrahedra and the wall-model mesh is generated by extruding the wall zone of LES mesh, there is no guarantee that top matching faces in the wall-model mesh will have their exact counterparts in the LES mesh. When the wall-model mesh is built independently of the LES mesh, even the wall faces might not be shared between solvers. For this purpose, an interprocessor face mapping across two solvers is created at the pre-processing stage of simulations, and non-blocking MPI routines are used for efficient BC communications. The following summarizes the face mapping and associated interpolation of BC in the most general situation, for any given quantity $\phi$:

- Wall-face mapping: For each LES wall face `ifa_w_les`, find a RANS wall face `ifa_w_rans` that lies closest to it based on the distance between face centers. Then $\nabla\phi$ at the face center of `ifa_w_les` is reconstructed from the wall-model solution using $\nabla\phi_{icv0}$, $\phi_{icv0}$, and $\phi_{wall}$, where $icv0$ denotes the wall boundary cell associated with `ifa_w_rans`.
- Matching-face mapping: For each top boundary face of RANS `ifa_t_rans`, find an internal face of LES `ifa_les` that lies closest to it based on the distance between face centers. The face `ifa_les` will have two associated internal cells. For each of them, calculate the distance from its cell center to the face center of `ifa_t_rans`. Denote the cell with the smaller distance with $icv0$. Then $\phi$ at the face center of `ifa_t_rans` is reconstructed from the LES solution ($\phi_{icv0}$ and $\nabla\phi_{icv0}$), using a truncated second order Taylor expansion.

### 2.4. *Cost*

In the test cases considered in Section 3, the ratio of the number of cells in the wall-model to the number of cells in the LES was about 0.2-0.5, and the extra cost of solving the wall-model equations was about 100-150% of the stand-alone LES. Compared to an additional 30% cost of the equilibrium wall-model implemented in a similar code (Bodart & Larsson 2012), the cost of the present WMLES formulation is significantly higher. This is mainly because of the inversion of a large matrix system in implicit time advancement. However, we anticipate that non-equilibrium effects important in complex flows could be better represented with the current formulation.

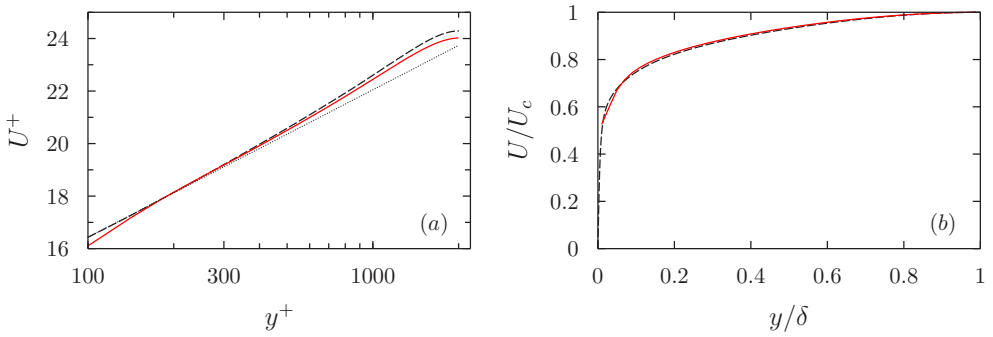


FIGURE 1. Mean streamwise velocity profile in (a) wall coordinates and (b) global coordinates. $U_c$ is the channel center-line velocity. Red solid line, present WMLES; dashed line, DNS of Hoyas & Jiménez (2006); dotted line, log-law ($\kappa = 0.41$, $B = 5.2$).

## 3. Validation

### 3.1. *Turbulent channel flow*

#### 3.1.1. *Computational setup*

We first consider the classical turbulent channel flow as the simplest test case without pressure gradient effects. DNS of Hoyas & Jiménez (2006) is used here as a reference. Simulation is performed at $Re_\tau = 2000$, the Reynolds number based on the channel half-height $\delta$, the friction velocity $u_\tau$, and the kinematic viscosity $\nu = \mu/\rho$. The size of the computational domain is $L_x = 25\delta$, $L_y = 2\delta$, and $L_z = 10\delta$ in the streamwise ($x$), wall-normal ($y$), and spanwise ($z$) directions, respectively. This is comparable to the domain size used in the DNS ($L_x = 8\pi\delta$, $L_y = 2\delta$, and $L_z = 3\pi\delta$). The uniform grid spacings in wall units in each direction are $(\Delta x^+,\ \Delta y^+,\ \Delta z^+) = (200,\ 40,\ 125)$. The number of grid points in the LES totals 4 million with $(N_x,\ N_y,\ N_z) = (250,\ 100,\ 160)$. The matching plane is located at $y^+ = 200$. The wall-model mesh has the same wall-parallel grid spacings as the LES mesh, but has 30 stretched cells for each channel wall, amounting to a total of 2.4 million cells. There is a factor of 2,800 saving in terms of the number of grid points compared to the DNS. A constant mass flow rate, deduced from the DNS mean velocity profile, is enforced by dynamically adjusting the source terms in the streamwise momentum and energy equations. Periodic boundary conditions are applied in the streamwise and spanwise directions, and the wall temperature is kept constant at the reference temperature. The Mach number at the center line is 0.2.

#### 3.1.2. *Results*

Comparisons of the mean and rms velocity fluctuations predicted by the wall-modeled LES and those from the DNS show good agreement. In Figure 1, the mean streamwise velocity is plotted against the distance from the wall using the inner and outer scalings. Except for a small discrepancy in the wake region, the agreement is satisfactory. Figure 2 shows the distribution of the resolved part of the Reynolds stress tensor across the channel. All normal components are underpredicted in the outer layer. The discrepancy would be reduced if the contribution of the sub-grid scale stresses were added to the resolved portion of the Reynolds stresses captured by LES.

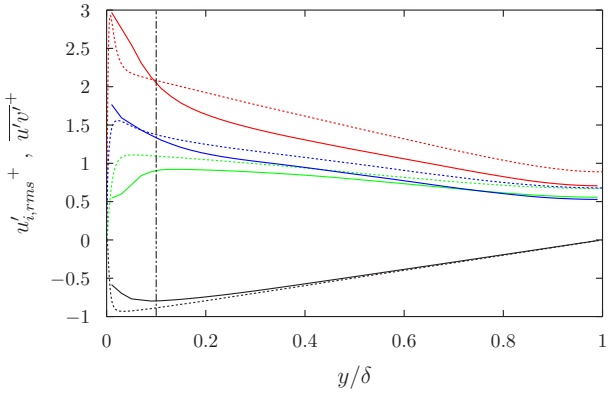


FIGURE 2. (Resolved) Reynolds stresses. Solid lines, present WMLES; dashed lines, DNS of Hoyas & Jiménez (2006); dashed-dotted line, matching location in present WMLES.

| $L_x$ | $L_y$ | $L_z$ | $N_x$ | $N_y$ | $N_z$ | $\Delta x \times 10^5$ | $\Delta y_1 \times 10^5$ | $\Delta z \times 10^5$ | $Re_\theta$ |
|---|---|---|---|---|---|---|---|---|---|
| 21.6 | 1.5 | 0.15 | 745 | 115 | 16 | $2000 \sim 4300$ | $20 \sim 800$ | 937.5 | $200 \sim 3300$ |

TABLE 1. LES mesh information of an H-type simulation. $\Delta y_1$ is the cell-center-to-wall distance of the wall-adjacent cells.

### 3.2. *Transitional boundary layer*

#### 3.2.1. *Computational setup*

We now consider a transitional boundary layer flow over a flat plate. The DNS of an H-type transition to turbulence by Sayadi *et al.* (2013) is used as a reference. In this flow, resonant interaction between the two-dimensional Tollmien-Schlichting (TS) wave and the spanwise oblique wave leads to the staggered formation of $\Lambda$ vortices, which eventually break down into turbulence. This is a more challenging test case than a fully turbulent boundary layer since the wall-model should predict the correct laminar/turbulent transition point and the overshoot in the skin friction. A dynamic wall-model sensor based on the turbulent kinetic energy level (at the matching location) proposed by Bodart & Larsson (2012) is adopted here to revert to the no-slip condition and to switch off the RANS eddy viscosity in the laminar region.

Details of the LES computational domain are given in Table 1. The size of the computational domain is $1 \leq x/x_0 \leq 22.6$ in the streamwise direction, $0 \leq y/x_0 \leq 1.5$ in the wall-normal direction, and $0 \leq z/x_0 \leq 0.15$ in the spanwise direction. Here the reference length scale $x_0$ is the distance of the inlet station from the virtual leading edge at $x = 0$. The inlet Reynolds number at $x = x_0$ based on the kinematic viscosity ($\nu = 10^{-5}$) and the free-stream velocity ($U_\infty = 1$) is $10^5$. Compared to Sayadi *et al.* (2013), the domain has been lengthened by a factor of two in the streamwise direction. The spanwise domain length is equal to the wavelength of the oblique wave, $\lambda_0/x_0 = 0.15$. In order to capture the correct streamwise growth of the disturbance waves, fine resolution is needed in the laminar region (otherwise the flow stays laminar). Therefore, grid spacings ($\Delta x/x_0 = 0.02$ and $\Delta y_1/x_0 = 2 \times 10^{-4}$) are kept constant up to $x/x_0 = 6.3$, where $\Delta y_1$ is the cell-center height of the wall-adjacent cells. From $x/x_0 = 6.3$, the grid is smoothly

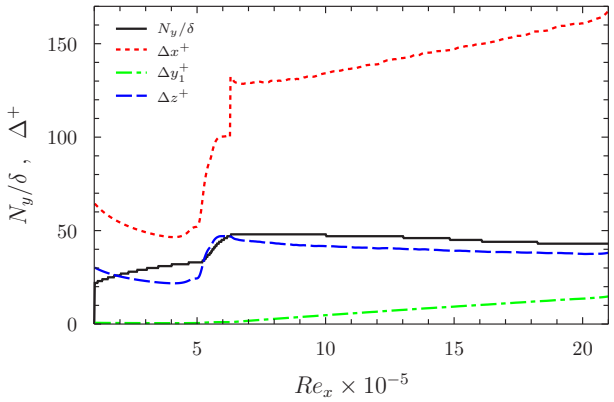


FIGURE 3. LES mesh resolution in terms of grid spacings in wall units ($\Delta^+$) and the number of cells below the boundary layer thickness ($N_y/\delta$). Quantities are based on the *local* skin friction velocity and boundary layer thickness. Black solid line, $N_y/\delta$; red dashed line, $\Delta x^+$; green dashed-dotted line, $\Delta y_1^+$; blue long-dashed line, $\Delta z^+$;

stretched in both streamwise and wall-normal directions (see Figure 3). Note that $N_y/\delta$ in the fully turbulent region is kept roughly constant at 45. It can be also deduced from Figs. 3 and 5 that $N_x/\delta \approx 10$ and $N_z/\delta \approx 25$ in the turbulent region. Therefore, the near-wall resolution in the turbulent region is still very coarse, and a wall-model is required. The wall-model mesh has the same wall-parallel dimensions and grid spacings as the LES mesh, but has only 25 cells in the wall-normal direction. The exchange location is placed at roughly 10% of the local boundary layer thickness (see Figure 5). The number of cells in the LES and the wall-model totals 1.4 million and 0.3 million, respectively. In terms of the resolution in the turbulent region, there is a factor of 600 saving compared to the DNS.

The TS and oblique waves are introduced within a narrow strip between $x_1/x_0 = 1.6$ and $x_2/x_0 = 1.8$. Following Sayadi *et al.* (2013), the wall-normal velocity within the disturbance strip is given by the blowing and suction boundary condition,

$$\frac{v(x,z,t)}{U_\infty} = A_1 f(x)\sin(\omega t) + A_{1/2} f(x) g(z)\sin(\omega t/2), \tag{3.1}$$

$$f(x) = \epsilon(15.1875\xi^5 - 35.4375\xi^4 + 20.25\xi^3), \tag{3.2}$$

$$\xi = \begin{cases} \frac{x-x_1}{x_m-x_1} & \text{if } x_1 \le x \le x_m \\ \frac{x_2-x}{x_2-x_m} & \text{if } x_m \le x \le x_2, \end{cases} \tag{3.3}$$

where $x_m = (x_1+x_2)/2$, $\epsilon = \text{sign}(x_m - x)$, $g(z) = \cos(2\pi z/\lambda_0)$, $A_1 = 1.044 \times 10^{-3}$, and $A_{1/2} = A_1/20$. The non-dimensional frequency is $F = 1.24 \times 10^{-4}$, where $F = \omega\nu/u_\infty^2$. The values of $A_1$ and $A_{1/2}$ are chosen such that the initial modal growth partially matches the experiment of Kachanov & Levchenko (1984).

The initial condition is the self-similar solution of the compressible laminar boundary layer equations. Periodic boundary conditions are used along the spanwise direction. The wall is assumed to be thermally adiabatic, and the freestream Mach number is $M_\infty = 0.2$. To prevent unphysical reflection of the outgoing waves and allow turbulent structures to leave the domain smoothly, the computation domain is covered by a numerical sponge (Mani 2012). Reference data to which the solution inside the sponge region is damped

are a laminar solution at the inlet and the top, and a time-averaged solution computed on the fly at the outlet. The sponge is active at all $y$ for $1 \leq x/x_0 \leq 1.5$ and $x/x_0 \geq 21.1$. For the remaining region the sponge is active for $y/x_0 \geq 1.2$.

#### 3.2.2. *Results*

Figure 4(a) shows the skin friction coefficient $C_f = 2\tau_w/\rho U_\infty^2$ versus $Re_x$ from WMLES. Shown together are the results from the DNS (Sayadi *et al.* 2013) and a LES with no wall-model (Sayadi & Moin 2012). The latter used the dynamic Smagorinsky model with the same mesh resolution as the current WMLES up to $x = 6.3$, and finer $\Delta x$, $\Delta y_1$ in $x/x_0 > 6.3$, but underpredicts the skin friction in the overshoot region and beyond. This underprediction is attributed to the SGS model not producing sufficient Reynolds shear stress on this coarse grid (Sayadi & Moin 2012). In WMLES, the wall-model fills this gap by accounting for the unresolved inner-layer physics. Although the transition takes place a little earlier than in the DNS, the overshoot in the skin friction and its subsequent decrease are captured by the wall-model. Note that the skin friction, including the laminar part, is entirely computed from the wall-model. The dynamic wall-model sensor of Bodart & Larsson (2012) successfully detects the transition and allows the wall-model to switch to the laminar equations when it should. As shown in Park *et al.* (2012) and Sayadi *et al.* (2013), statistics of fully developed turbulence are independent of transition routes. This is again confirmed in Figure 4(b), where $C_f$ is plotted against $Re_\theta$ together with the results from a wall-resolved LES of a boundary layer up to $Re_\theta = 4300$ (Schlatter *et al.* 2010) and a DNS of bypass transition up to $Re_\theta = 1840$ (Wu & Moin 2010). Here, $Re_\theta$ is more relevant than $Re_x$ as a streamwise coordinate since it quantifies the momentum loss regardless of physical location on the plate. Although transition triggered by different means (such as tripping body force (Schlatter *et al.* 2010) and isotropic turbulence boxes migrating periodically in the free-stream (Wu & Moin 2010)) takes place in different locations, the skin friction in the developed state collapses into a single curve.

In Figure 5, the mean streamwise velocity profiles at five different locations ($Re_\theta =$ 1250, 1840, 2530, 2990 and 3310) are shown along with the reference DNSs (Sayadi *et al.* 2013; Wu & Moin 2010) and experimental data (Österlund 1999). Profiles are in good agreement. Log-layers with the correct slope and intercept are clearly found in all profiles. Reynolds stress profiles at $Re_\theta = 1840$ and $Re_\theta = 2560$ in Figure 6 also show good agreement with the published DNS and LES data.

### 3.3. *High Reynolds number turbulent boundary layer*

#### 3.3.1. *Computational setup*

The next test case is a high Reynolds number flat-plate boundary layer flow measured by DeGraaff & Eaton (2000). In their wind-tunnel experiments, turbulence statistics at $Re_\theta = 1430$, 2900, 5200, 13000, and 31000 were obtained with a high-resolution laser-Doppler anemometer (LDA) system. Here the focus is on the measurements at the highest Reynolds number ($Re_\theta = 31000$). Wall-resolved LES of this flow is not feasible owing to the high Reynolds number. This case is chosen to validate the proposed non-equilibrium wall-model at high Reynolds number, where Wang and Moin's model was reported not to perform satisfactorily (Kawai & Larsson 2013).

In terms of the inlet boundary layer thickness $\delta_r$, the dimension of the computational box is $(L_x, L_y, L_z) = (50\delta_r, 15\delta_r, 2\delta_r)$. Grid spacings in wall units are $(\Delta x^+, \Delta y_1^+, \Delta z^+) \approx (450, 120, 450)$, and there are approximately 45 cells within the boundary layer

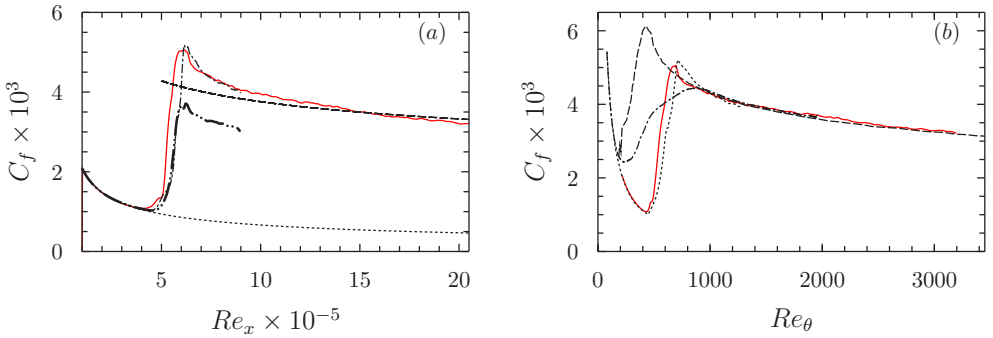


FIGURE 4. Skin friction along the flat plate. (a) Red solid line, present WMLES; dash-dotted line, DNS of Sayadi *et al.* (2013); dashed-dot-dotted line, LES of Sayadi & Moin (2012); dashed line, Blasius; long-dashed line, turbulent correlation (White 2006). (b) Red solid line, present WMLES; dashed line, DNS of Sayadi *et al.* (2013); dash-dotted line, DNS of Wu & Moin (2010); long-dashed line, resolved LES of Schlatter *et al.* (2010)

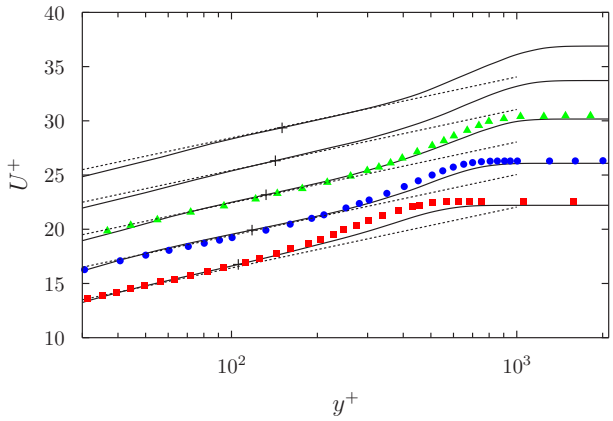


FIGURE 5. Mean velocity profile $U^+$ in viscous wall units at $Re_\theta = 1250$, 1840, 2530, 2990, and 3310 (from bottom to top). Profiles are shifted by $U^+ = 3$ along the ordinate for increasing $Re_\theta$. Solid lines, present WMLES; dashed line, log-law ($\kappa = 0.41$, $B = 5.2$); +, matching locations; ■ , DNS of Sayadi *et al.* (2013) at $Re_\theta = 1250$; ● , DNS of Wu & Moin (2010) at $Re_\theta = 1840$; ▲, experiment of Österlund (1999) at $Re_\theta = 2530$.

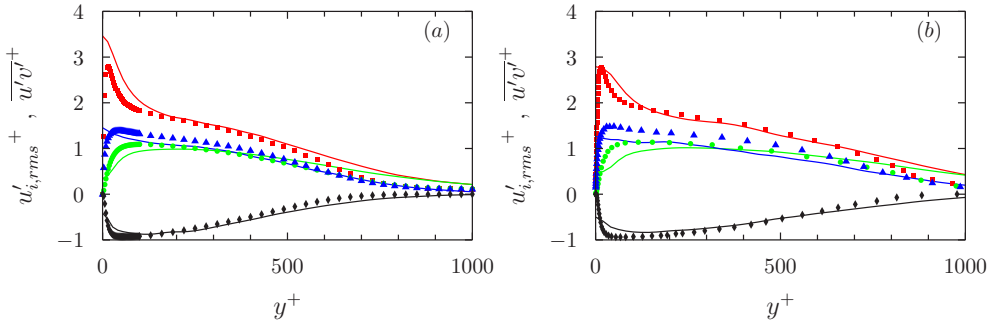


FIGURE 6. (Resolved) Reynolds stresses at (a) $Re_\theta = 1840$ and (b) $Re_\theta = 2560$. Lines are for the present WMLES. Symbols in (a) from DNS of Wu & Moin (2010) at $Re_\theta = 1840$, and symbols in (b) from wall-resolved LES of Schlatter *et al.* (2010) at $Re_\theta = 2560$.

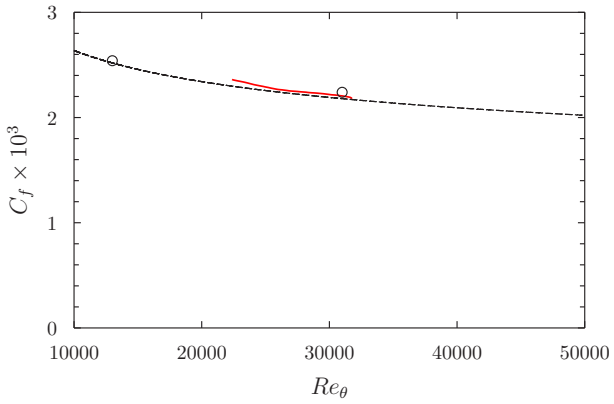


FIGURE 7. Skin friction along the flat plate. Red solid line, present WMLES; dashed line, empirical correlation of Fernholz & Finley (1996) ($C_f/2 = (2.5 \ln Re_\theta - 5.89)^{-2}$); ∘, experiment of DeGraaff & Eaton (2000).

thickness ($N_y/\delta = 45$). Cell densities in the wall-parallel directions deduced from Figure 8 are $N_x/\delta = N_z/\delta = 25$. The wall-model mesh has the same grid sizes as those of the LES mesh in the wall-parallel directions, but has 30 cells in the wall-normal direction. The matching plane is located at $y \approx 0.1\delta_r$. The number of cells in the LES and the wall-model mesh totals 2.9 million and 0.7 million, respectively.

Periodic boundary conditions are used along the spanwise direction. The wall is assumed to be thermally adiabatic, and the freestream Mach number is $M_\infty = 0.2$. The top and exit of the computational domain are covered by numerical sponges, in which the solution is damped to a local time-averaged solution. The sponge is active at all $x$ for $0.35 \leq y \leq 0.5175$ and at $x \geq 1.625$. The inlet Reynolds number based on the momentum thickness ($\theta$), the kinematic viscosity ($\nu = 2.88 \times 10^{-6}$), and the free-stream velocity ($U_\infty = 17.15$) is 22000. A turbulent inflow generation technique based on digital filtering (Klein *et al.* 2003) is used to provide the inflow boundary condition.

#### 3.3.2. *Results*

In Figure 7, the skin friction along the plate from WMLES is shown together with the experimental data and an empirical correlation for incompressible high Reynolds number boundary layers. In the experiment, the Reynolds number was varied by changing the ambient density and the free-stream velocity, so that there are only two data points (open circles) in this Reynolds number range. WMLES prediction is in very good agreement with the reference data. Figure 8 shows the mean streamwise velocity profile at $Re_\theta = 31000$ in wall coordinates and outer-layer coordinates. The velocity-defect profile is also included in Figure 8(b). The resolved Reynolds stress profiles are shown in Figure 9. The results are in excellent agreement with the experiment.

### 3.4. *Flow over a NACA4412 airfoil at near-stall conditions*

#### 3.4.1. *Computational setup*

The final case considered is the flow over a NACA4412 airfoil operating close to maximum lift. The corresponding angle of attack (AoA) is 12°, which was determined by Wadcock (1987) in a low-speed wind tunnel experiment. The Reynolds number based on the chord length and incident freestream velocity is $Re_c = U_\infty c/\nu_\infty = 1.64 \times 10^6$, and Mach number is $M_\infty = 0.2$. Although the Reynolds number is not very high, various

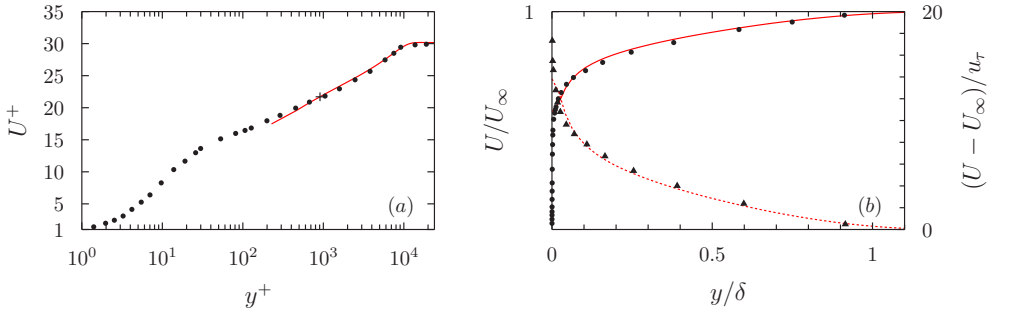


FIGURE 8. Mean streamwise velocity profile at $Re_\theta = 31000$ in (a) wall coordinates and (b) outer-layer coordinates. Lines, present WMLES; • and ▲, DeGraaff & Eaton (2000); +, matching location

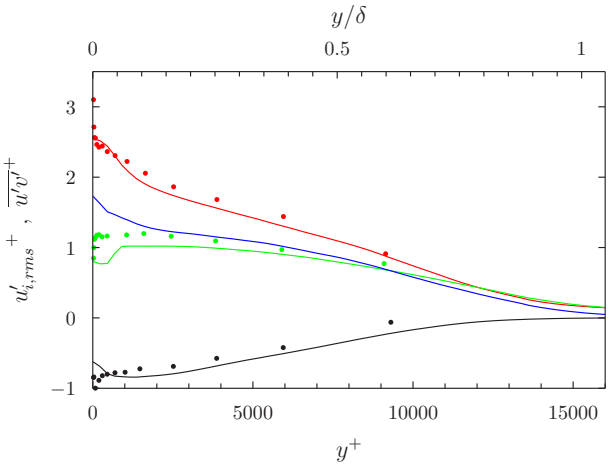


FIGURE 9. (Resolved) Reynolds stresses at $Re_\theta = 31000$. Lines are for the present WMLES and symbols (${u'_{rms}}^+$, ${v'_{rms}}^+$, and $\overline{u'v'}^+$) from DeGraaff & Eaton (2000).

flow features on the airfoil suction surface make it a challenging test case for WMLES. These include a thin laminar boundary layer developing from the stagnation point near the nose, transition to turbulence, trailing edge separation induced by adverse pressure gradient, and the mixing layer in the wake region. Notice that the boundary layer grows by a factor of 1000 along the upper surface, ranging from $\delta/c \sim 10^{-4}$ in the laminar region to $\delta/c \sim 0.1$ near the trailing edge. This scale separation imposes a prohibitive resolution requirement and a severe acoustic CFL restriction for a wall-resolved LES. A wall-model is needed.

Figure 10 shows the computational domain. The dimension of the computational box is $(L_X, L_Y, L_Z) = (9c, 2.37c, 0.72c)$. Wind tunnel walls are included to reproduce the blockage effect in the experiment. However, no attempt is made to resolve boundary layers on the tunnel walls, and they are modeled with slip-wall BC. The origin of the fixed simulation coordinate system $(X, Y)$ is defined at the (0, 0) point in Figure 10. Using the chordline position at AoA = 0° and the coordinate of pitch pivot-point provided by Wadcock (1987), the airfoil's relative position with respect to the tunnel walls is exactly reproduced. Coordinates of the leading and trailing edge of the airfoil are $(X, Y)$ = (0.0406, -0.02227) and (1.019, -0.2302), respectively. The inlet and outlet of the com-

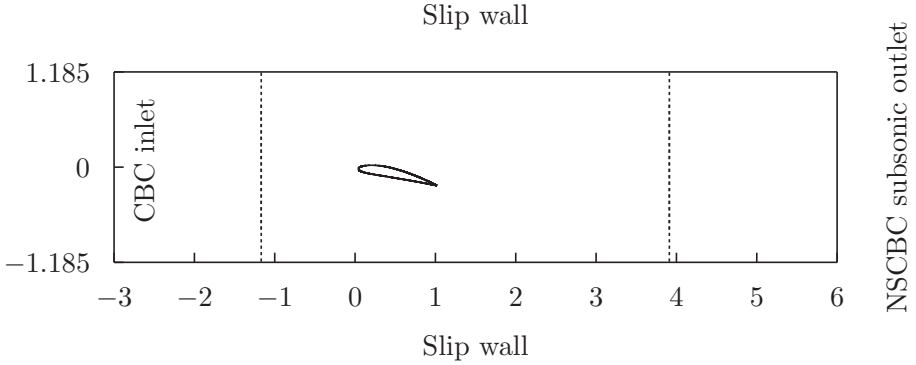


FIGURE 10. Computational domain and boundary conditions. Dashed lines indicate the start and end of the actual test section in Wadcock's experiment. Figure drawn to scale and length normalized by chord.

putational domain are placed farther away from the airfoil than those in the experiment, since they seemed to be too close to the airfoil (see Figure 10). Two additional coordinate systems are introduced for post-processing purposes only. The airfoil coordinate system $(x, y)$ is aligned with the chordline and chord-normal line, with its origin placed at the leading edge. The wake coordinate system $(x_w, y_w)$ is aligned with the simulation coordinate system, but its origin is placed at the trailing edge. The experiment reports boundary layer and wake profiles at $x/c = 0.529$, 0.815, 0.925 and $x_w/c = 0.007$, 0.282.

The number of cells in the LES and the wall-model mesh totals 10.7 million and 2.7 million, respectively. The LES mesh was generated from a very coarse mesh by refining it locally with the adaptation tool *adapt*. On the airfoil suction surface, the grid spacing in the tangential direction is $\Delta^{||}/c = 2.5 \times 10^{-4} \sim 6 \times 10^{-3}$. Spanwise resolution near the wall is fixed at $\Delta z/c = 0.001$. The wall-normal grid spacing of wall-boundary cells is fixed at $\Delta^{\perp}/c = 2 \times 10^{-4}$.

In WMLES, relevant parameters characterizing the grid resolution are the number of cells within the local boundary layer thickness in each direction. Figure 11 illustrates the distribution of cell densities in each direction on the suction surface. For the first 60% of the airfoil, cell densities in tangential and spanwise directions are very low ( $< 20$), then they rise steeply after $x/c = 0.7$ due to the rapid growth of boundary layer close to separation. This does not necessarily translate into a waste of resolution in the rear part, since the separated shear layer still seems to need a decent resolution. Cell density in the wall-normal direction is much higher than in the other two, but only one cell is used to represent the laminar boundary layer near the nose. It could be lowered if the mesh was built in such a way that wall-normal resolution could vary along the streamwise direction. However, we emphasize that average cell densities obtained by integrating the curves in Figure 11 over $x/c$ are $(\bar{n}_{||}, \bar{n}_{\perp}, \bar{n}_z) \approx (17, 37, 31)$, which conforms well to the standard suggested by Choi & Moin (2012).

The initial condition is a uniform velocity field $(U_\infty, 0, 0)$ superimposed with a random noise field (5% of $U_\infty$) in the vicinity of the airfoil. A uniform freestream is imposed at the inlet using characteristic boundary conditions (CBC), and the subsonic-outlet Navier-Stokes CBC of Poinsot & Lele (1992) are used at the outlet. Periodic boundary conditions are used along the spanwise direction. The wall is assumed to be thermally adiabatic. Flow statistics are gathered over more than 4 convective time scales ($\tau_c = c/U_\infty$), after waiting for more than $12\tau_c$.

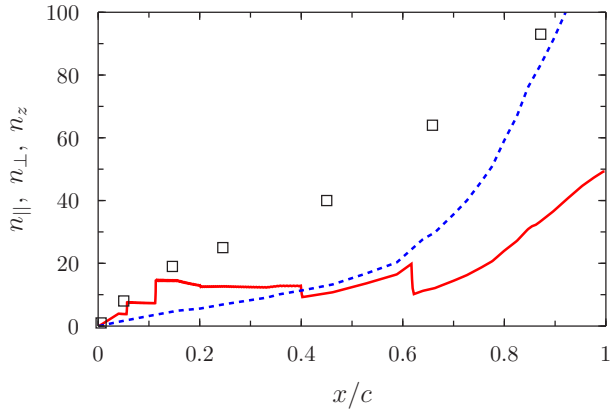


FIGURE 11. Number of boundary-layer-resolving cells in tangential ($n_{||}$, red solid line), wall-normal ($n_\perp$, square), and spanwise directions ($n_z$, blue dashed line).

3.4.2. *Results*

Figure 12 shows the mean streamwise velocity profiles on the upper surface and in the wake region. Notice that boundary layer profiles (solid lines) are measured along local normals to the upper surface, while wake profiles (dashed-dotted lines) are measured along normals to the wind tunnel axis. Therefore, the corresponding distance variable $\eta$ in the ordinate axes of Figure 12 is the wall-normal and axis-normal distances, respectively. Figure 13 shows the normal component of mean velocity at the same probe locations.

Streamwise velocity from WMLES is in very good agreement with the experimental measurements. Although the measurement provides only three probe lines on the suction surface, it can be reliably assumed that boundary layer growth along the suction surface is nicely reproduced. The boundary layer clearly separates at the trailing edge. Maximum reverse flow velocity at $x/c = 0.952$ is $-0.157U_e$, where $U_e$ is the tangential velocity at the boundary layer edge. This value is very close to $-0.16U_e$ reported by Wadcock (1987). The merging of the two shear layers into an asymmetric wake is also well predicted. A reasonable prediction of the wall-normal velocity can be observed on the suction surface. However, the agreement in the wake region is not satisfactory.

Figure 14 shows the average pressure coefficient $C_p = 2(P - P_\infty)/(\rho U)^2_\infty$ on the airfoil surface. Flattening of $C_p$ near the trailing edge due to the flow retardation is well captured. Pressure minimum on the suction surface is slightly underpredicted, implying that the local flow velocity there is overpredicted. It is suspected that the wall stress is underpredicted in this laminar region because of the insufficient grid resolution. A small discrepancy in the suction side pressure coefficient persists up to $x/c \approx 0.3$, but overall agreement with the experiment is acceptable.

## 4. Conclusion and future work

A non-equilibrium wall-model for LES based on 3D unsteady RANS equations has been implemented and partially validated. This work builds on previously proposed non-equilibrium wall-models, but with important differences. First, the wall- model is implemented in a fully unstructured mesh environment. To the authors knowledge, this is the first implementation of a non-equilibrium model in an unstructured solver. Second, the present wall-model is equipped with a new dynamic turbulence closure for eddy viscos-

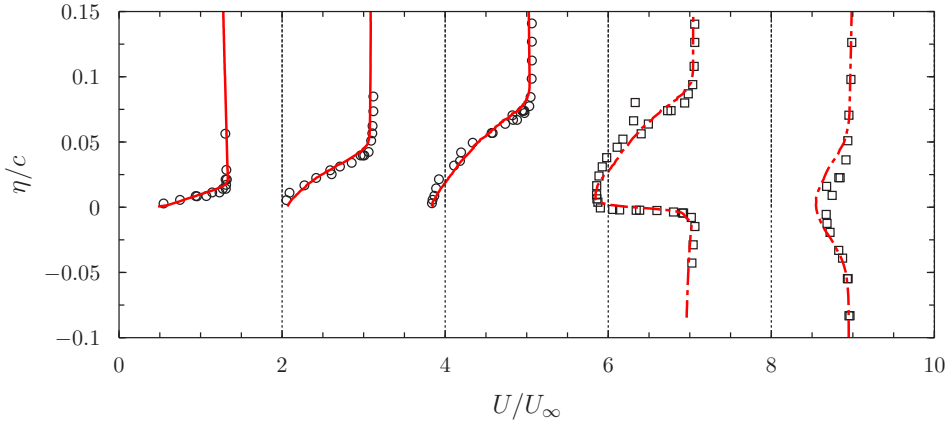


FIGURE 12. From left to right, mean velocity component tangential to the airfoil suction surface at $x/c = 0.529$, 0.815, 0.952 (solid lines and circles), and velocity component parallel to the tunnel axis in the wake at $x_w/c = 0.007$, 0.282 (dashed-dotted lines and squares). Profiles are shifted by 0, 2, $\cdots$, 8 along the abscissa. Lines are for the present WMLES and symbols are from Wadcock (1987).

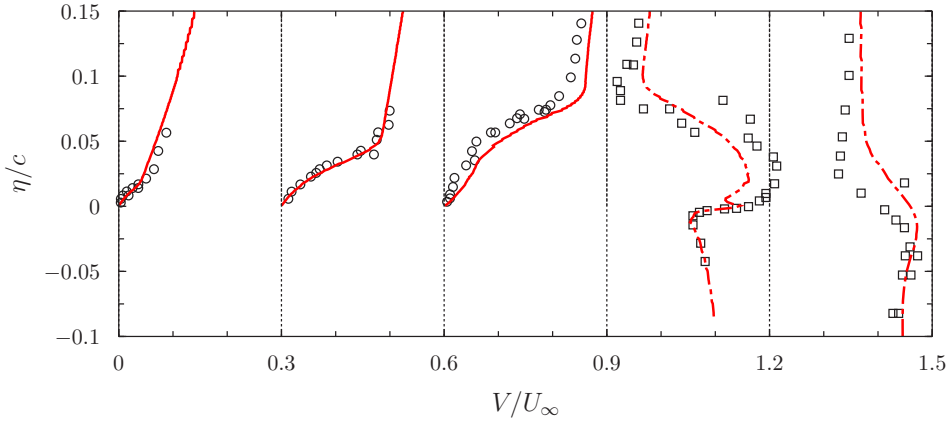


FIGURE 13. From left to right, mean velocity component normal to the airfoil suction surface at $x/c = 0.529$, 0.815, 0.952 (solid lines and circles), and velocity component normal to the tunnel axis in the wake at $x_w/c = 0.007$, 0.282 (dashed-dotted lines and squares). Profiles are shifted by 0, 0.3, 0.6, 1.2, and 1.5 along the abscissa. Lines are for the present WMLES and symbols are from Wadcock (1987).

ity/conductivity. The proposed model senses the local state of the resolved stress and uses this information to dynamically adjust the model coefficients, without resorting to a tunable parameter or stress matching procedure.

The proposed non-equilibrium wall-model was partially validated against canonical attached turbulent flows at a wide range of Reynolds numbers, and a flow over a NACA4412 airfoil at near-stall condition. Predictions of the low-order statistics from the wall-modeled LES were in good agreement with the reference calculations and experiments.

In order to establish the credibility and applicability of the present wall-model, it has to be tested against more challenging flows. An ideal test case should involve a high Reynolds number inhomogeneous flow in or over engineering devices, and have good

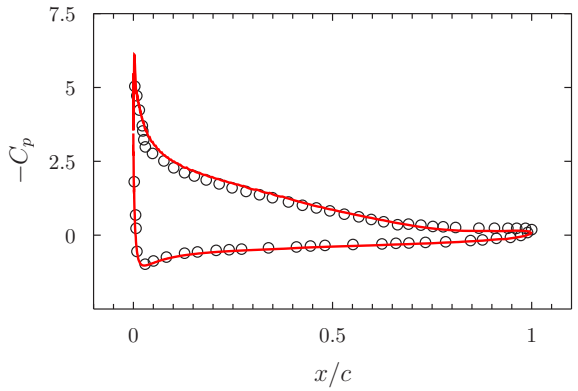


FIGURE 14. Pressure distribution along the airfoil surface. Lines are for the present WMLES and symbols are from Wadcock (1987).

reference data available (high-fidelity simulations or measurements). This is somewhat rare, and currently we are seeking good test cases to validate the wall-model.

## Acknowledgments

This work was supported by the Winston and Fu-Mei Stanford Graduate Fellowship and NASA Aeronautics Scholarship Program, and in part by the NASA under the Subsonic Fixed-Wing Program (Grant NNX11AI60A) and the Boeing Company. The authors are grateful to Dr. Ivan Bermejo-Moreno for his valuable comments on a preliminary version of this manuscript.

## REFERENCES

BALARAS, E., BENOCCIS, C. & PIOMELLI, U. 1996 Two-layer approximate boundary conditions for large-eddy simulations. *AIAA J.* **34**, 1111–1119.

BODART, J. & LARSSON, J. 2012 Sensor-based computation of transitional flows using wall-modeled large eddy simulation. In *Annual Research Briefs*, pp. 229–240. Center for Turbulence Research.

CABOT, W. & MOIN, P. 2000 Approximate wall boundary conditions in large-eddy simulation of high Reynolds number flow. *Flow, Turbulence, and Combustion* **63**, 269–291.

CHOI, H. & MOIN, P. 2012 Grid-point requirements for large eddy simulation: Chapman's estimates revisited. *Phys. Fluids* **24**, 011702.

DEGRAAFF, D. B. & EATON, J. K. 2000 Reynolds-number scaling of the flat-plate turbulent boundary layer. *J. Fluid Mech.* **422**, 319–346.

FERNHOLZ, H. H. & FINLEY, P. J. 1996 The incompressible zero-pressure-gradient turbulent boundary layer: An assessment of the data. *Prog. Aerospace Sci.* **32**, 245–311.

HAM, F. & IACCARINO, G. 2004 Energy conservation in collocated discretization schemes on unstructured meshes. In *Annual Research Briefs*, pp. 3–14. Center for Turbulence Research.

HOYAS, S. & JIMÉNEZ, J. 2006 Scaling of the velocity fluctuations in turbulent channels up to $Re_\tau = 2003$. *Phys. Fluids* **18**, 011702.

Kachanov, Y. S. & Levchenko, V. Y. 1984 The resonant interaction of disturbances at laminar-turbulent transition in a boundary layer. *J. Fluid Mech.* **138**, 209–247.

Kawai, S. & Larsson, J. 2013 Dynamic non-equilibrium wall-modeling for large eddy simulation at high Reynolds numbers. *Phys. Fluids* **25**, 015105.

Khalighi, Y., Nichols, J. W., Ham, F., Lele, S. K. & Moin, P. 2010 Unstructured large eddy simulation for prediction of noise issued from turbulent jets in various configurations. *17th AIAA AIAA/CEAS Aeroacoustics Conference, 6-8 Jun 2010, Portland, Oregon* .

Klein, M., Sadiki, A. & Janicka, J. 2003 A digital filter based generation of inflow data for spatially developing direct numerical or large eddy simulations. *J. Comput. Phys.* **186**, 652–665.

Lilly, D. K. 1992 A proposed modification of the Germano subgrid-scale closure method. *Phys. Fluids A* **4**, 633–635.

Mani, A. 2012 Analysis and optimization of numerical sponge layers as a nonreflective boundary treatment. *J. Comput. Phys.* **231**, 704–716.

Moin, P., Squires, K., Cabot, W. & Lee, S. 1991 A dynamic subgrid-scale model for compressible turbulence and scalar transport. *Phys. Fluids* **3**, 2746.

Österlund, J. M. 1999 Experimental studies of zero pressure-gradient turbulent boundary layer flow. PhD dissertation, Royal Institute of Technology, KTH, Stockholm.

Park, G. I. & Moin, P. 2014 An improved dynamic non-equilibrium wall-model for large eddy simulation. *Phys. Fluids* (in press).

Park, G. I., Wallace, J. M., Wu, X. & Moin, P. 2012 Boundary layer turbulence in transitional and developed states. *Phys. Fluids* **24**, 035105.

Pečnik, R., Terrapon, V. E., Ham, F. & Iaccarino, G. 2010 Full-system RANS of the Hyshot II scramjet. part 1: Numerics and non-reactive simulations. In *Annual Research Briefs*, pp. 57–68. Center for Turbulence Research.

Piomelli, U. 2008 Wall-layer models for large-eddy simulations. *Prog. in Aero. Sci.* **44**, 437–446.

Piomelli, U. & Balaras, E. 2002 Wall-layer models for large-eddy simulations. *Annu. Rev. Fluid Mech.* **34**, 349–374.

Poinsot, T. J. & Lele, S. K. 1992 Boundary conditions for direct simulations of compressible viscous flows. *J. Comput. Phys.* **101**, 104–129.

Sayadi, T., Hamman, C. W. & Moin, P. 2013 Direct numerical simulation of complete H-type and K-type transitions with implications for the dynamics of turbulent boundary layers. *J. Fluid Mech.* **724**, 480–509.

Sayadi, T. & Moin, P. 2012 Large eddy simulation of controlled transition to turbulence. *Phys. Fluids* **24**, 114103.

Schlatter, P., Li, Q., Brethouwer, G., Johansson, A. V. & Henningson, D. S. 2010 Simulations of spatially evolving turbulent boundary layers up to $Re_\theta = 4300$. *Int. J. Heat Fluid Flow* **31**, 251–261.

Wadcock, A. J. 1987 Investigation of low-speed turbulent separated flow around airfoils. *NASA contractor report 177450* .

Wang, M. & Moin, P. 2002 Dynamic wall modeling for large-eddy simulation of complex turbulent flows. *Phys. Fluids* **14**, 2043–2051.

White, F. M. 2006 *Viscous Fluid Flow*, 3rd edn. McGraw-Hill.

Wu, X. & Moin, P. 2010 Transitional and turbulent boundary layer with heat transfer. *Phys. Fluids* **22**, 085015.